Co-Regulating Planar Mg Deposition and Bromine-Rich Mg Anode-Electrolyte Interface by Multifunctional Organic Bromine Additive

Deviprasath Chinnadurai, Sonal Kumar, Chang Zhang, Man-Fai Ng, Yuanjian Li, Jianbiao Wang, Tanmay Ghosh, Gaoliang Yang, Zhenxiang Xing, Wei Liu, and Zhi Wei Seh**

D. Chinnadurai, S. Kumar, Y. Li, J. Wang, T. Ghosh, G. Yang, Z. Xing, Z. W. Seh

Institute of Materials Research and Engineering (IMRE),

Agency for Science, Technology and Research (A∗STAR),

2 Fusionopolis Way, Innovis #08-03, Singapore 138634, Republic of Singapore.

E-mail: sehzw@imre.a-star.edu.sg

C. Zhang, W. Liu

School of Physical Science and Technology,

ShanghaiTech University,

Shanghai 201210, People's Republic of China.

E-mail: liuwei1@shanghaitech.edu.cn

M.-F. Ng

Institute of High Performance Computing (IHPC),

Agency for Science, Technology and Research (A*STAR),

1 Fusionopolis Way, #16-16 Connexis, Singapore 138632, Republic of Singapore.

D.C., S.K., C.Z., contributed equally to this work.

Keywords: Magnesium batteries, Organic bromine additive, Planar Mg deposition, Br-rich SEI, High areal capacity cycling.

Abstract

Rechargeable magnesium batteries (RMBs) are highly promising candidates for next-generation energy storage systems due to their superior energy density and intrinsic safety. However, severe Mg anode passivation in conventional electrolytes and non-uniform Mg deposition significantly compromise their reversibility and cycling stability. Here, for the first time, we introduce a multifunctional 1-bromooctane (OctylBr) additive into the strongly passivating magnesium bis(hexamethyldisilazide) ($Mg(HMDS)_2$) electrolyte to engineer a Br-enriched solid electrolyte interphase (SEI) and promote uniform planar Mg deposition. This strategic electrolyte modification extends the Mg cycling lifespan of conventional electrolytes from 0 to 3600 hours with an exceptionally low overpotential of 45 mV in symmetric cell and a high coulombic efficiency of 99.34 % in asymmetric cell. The planar deposition enabled by our electrolyte allows for reversible Mg plating/stripping across a broad range of areal capacities (0.5–25 mAh/cm^2). Notably, at high areal capacity of 10 mAh/cm^2, the electrolyte sustains a lifespan of 640 hours in symmetric cell, underscoring its effectiveness for high-energy applications. Full-cell evaluations with Mo_6S_8 cathodes further validate the enhanced cycling performance, and the approach proves effective across various conventional Mg salts. These findings position OctylBr as a generally compatible electrolyte additive, unlocking new pathways for high-performance, long-life RMBs.

1. Introduction

The rechargeable Mg battery (RMB) is a promising "beyond Li" technology that is cheaper and safer than its Li-based counterpart. Such batteries typically employ a Mg metal anode that exhibits a large volumetric capacity (3833 mAh cm^{-3}) and a low reduction potential (-2.37 V versus standard hydrogen electrode (SHE)) that is paired with an intercalation or conversion cathode.[1] The passivation of the Mg anode surface in conventional electrolytes drastically impairs the reversibility and kinetics of the Mg deposition/stripping process, making this a major hurdle in developing practical RMBs. To mitigate this problem, there have been substantial efforts to create a robust solid electrolyte interface (SEI) with better Mg cycling properties that includes designing an artificial interphase[2-6] and establishing an SEI with electrolyte additives.[7-11]

Besides regulating the formation of SEIs, the generally low areal capacities of Mg anodes (0.02-1 mAh/cm^2) in conventional electrolytes also greatly hinder the practicability of RMBs.[12-15] Achieving high areal capacity in Mg electrodes requires homogenous Mg^{2+} flux distribution under a single cycle, the presence of many nucleation sites, and low voltage hysteresis.[16] However, in traditional electrolytes, the Mg anodes exhibit high inhomogeneity during Mg deposition which eventually results in a short circuit.[17] The higher charge density of Mg^{2+} leads to higher de-solvation energy and polarization in Mg anodes, resulting in charge accumulation and uneven electric field distribution on the electrode surface during prenucleation. This limits the distribution homogeneity of Mg^{2+} at nucleation sites, and as a result, hampers self-diffusion and prevents homogeneity in Mg plating. This makes it vital that the desired Mg deposition morphology be achieved with extremely homogenous electric fields and Mg^{2+} flux distributions.

To this end, highly concentrated metal chloride salts like $MgCl_2$ and $AlCl_3$ are the additives most widely used for modifying Mg electrolytes, which yields a $MgCl_2$-based SEI

component in common.[18-20] The use of Cl^- helps to break the native oxide layer but corrodes the cell components, a problem that can be mitigated by using other less corrosive Mg-halides (MgI_2, MgF_2, and $MgBr_2$) instead.[5, 21-23] In a previous study, we extensively investigated a series of inorganic Mg halides as electrolyte additives to overcome passivation and improve cycling life.[24] The results indicate that $MgBr_2$ additive performs the best among the Mg halides due to the lower activation energy and improved diffusion properties of Mg^{2+} in the SEI layer. However, the ionic nature of $MgBr_2$ leads to poor solubility in conventional ether-based electrolytes, resulting in inferior cycling life. In comparison, organic bromine liquid additives are covalent in nature and have generally high miscibility with ether solvents, which inspired us to study this class of less-explored additives.

In this work, for the first time, we used an organic 1-bromooctane (OctylBr) additive with a conventional electrolyte salt ($Mg(HMDS)_2$) for high-capacity and reversible Mg metal batteries. To the best of our knowledge, OctylBr has not been previously reported as an electrolyte additive for Mg batteries. The Br-rich SEI formed in situ that is facilitated by the OctylBr additive suppressed anode passivation effectively and improved cycling life substantially from 0 to 3600 hours, the longest reported to date for $Mg(HMDS)_2$ based electrolytes. The COMSOL simulation studies demonstrate that the additive-driven planar Mg deposition promotes the homogenous distributions of both electric field and Mg^{2+} flux at the electrode-electrolyte interface. As a result, the planar deposition morphology ensures reversible Mg cycling at a wide range of areal capacities (0.5-25 mAh/cm^2) with narrow overpotentials. A detailed analysis of passivation in $Mg(HMDS)_2$ electrolyte and SEI layer formation in $Mg(HMDS)_2$ + OctylBr electrolyte was conducted with theoretical and ex-situ analytical techniques. Our successful demonstration of reversible Mg cycling with other highly passivating conventional Mg salts ($Mg(OTf)_2$ and $Mg(TFSI)_2$) highlights the generality of OctylBr as an effective electrolyte additive for high-performance RMBs.

2. Results and discussion

2.1. Suppression of passivation and deposition regulation by OctylBr additive.

Conventional Mg electrolytes readily passivate at the surface of the Mg anode due to the spontaneous reduction of electrolyte components and decomposition of solvents, which result in low Mg-ion diffusion and high overpotential.[25-28] As predicted, the conventional electrolyte using 0.1 M $Mg(HMDS)_2$ salt in DME solvent (abbreviated as $Mg(HMDS)_2$) displayed typical Mg anode passivation, indicated by a rapid voltage drop to -3.2 V on initial plating **(Figure 1a).** To suppress this passivation, we modified the electrolyte by adding OctylBr to allow reversible Mg deposition/dissolution, as evidenced by the voltage profiles of the first cycle in Mg//Mg cells with different volumes of OctylBr added **(Figure S1)**. By understanding the electrochemical performance (**Figure S2-3**), we calculated that a 5 vol% of OctylBr additive is the optimal concentration for use with 0.1 M $Mg(HMDS)_2$; this is hereafter described as $Mg(HMDS)_2$ + OctylBr. The scanning electron microscopy (SEM) morphological study of initial Mg plating indicates that no Mg deposition occurred with the $Mg(HMDS)_2$ electrolyte, with many dead Mg sites seen **(Figure 1a-inset)**. However, homogeneous planar Mg deposition occurs with the $Mg(HMDS)_2$ + OctylBr electrolyte using a very low initial plating overpotential of only 0.28 V **(Figure 1b)**. To assess the unique effectiveness of the OctylBr additive in enhancing the reversibility of $Mg(HMDS)_2$ electrolyte, we investigated other octyl halides (OctylF, OctylCl, OctylI) as additives in both symmetric and asymmetric cells **(Figure S4)**. OctylF and OctylI failed to sustain cycling due to passivation. While OctylCl initially exhibited behavior similar to OctylBr, its long-term cycling life was significantly shorter. Additionally, electrolyte modified with inorganic bromide ($MgBr_2$) additive also failed to sustain cycling due to surface passivation **(Figure S5)**. These findings demonstrate the superiority of organic bromide (OctylBr) additives over inorganic counterparts and further highlight the advantages of bromine-based organic additives compared to other organic halides (Cl, F, I).

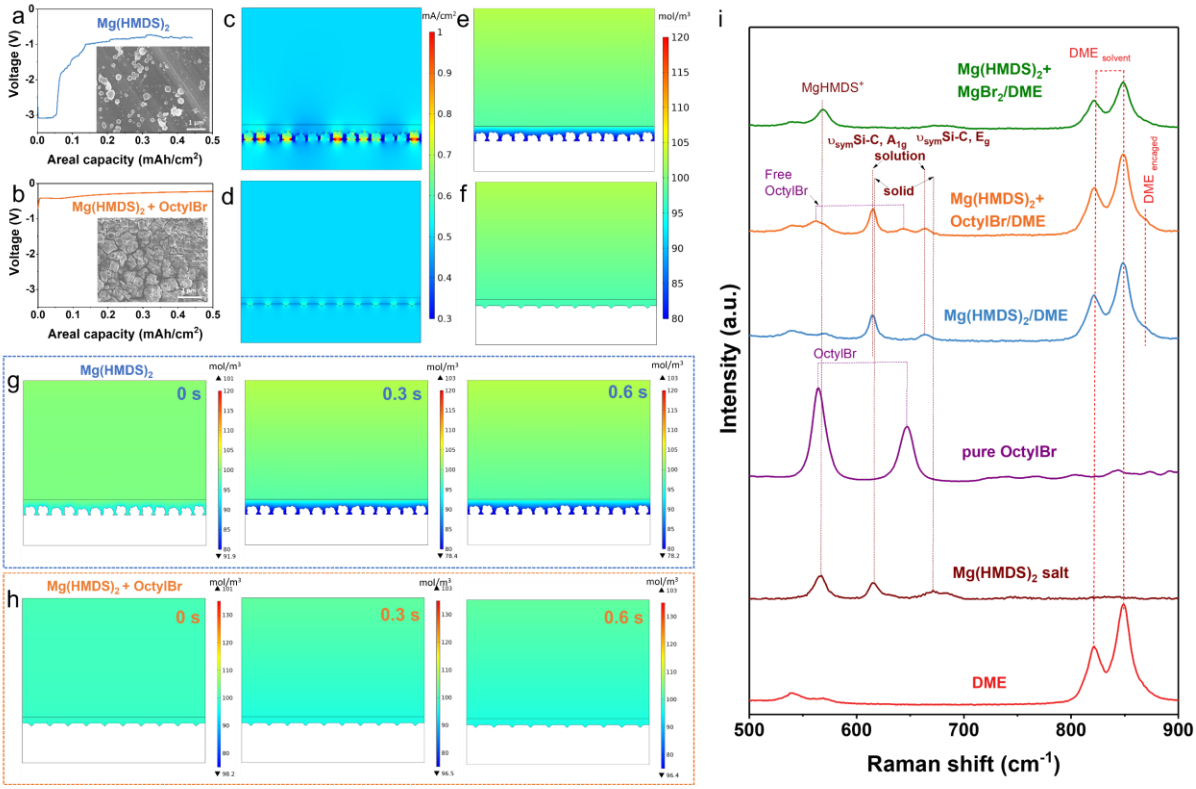

Figure 1. Voltage profile of initial plating in different electrolytes: (a) $Mg(HMDS)_2$, (b) $Mg(HMDS)_2$ + OctylBr, (a-b insets show corresponding SEM images). COMSOL simulations of electric field distribution in Mg deposits for different electrolytes: (c) $Mg(HMDS)_2$, (d) $Mg(HMDS)_2$ + OctylBr. COMSOL simulations of Mg^{2+} flux distribution in Mg deposits for different electrolytes: (e) $Mg(HMDS)_2$, (f) $Mg(HMDS)_2$ + OctylBr. The evolution of Mg^{2+} flux distribution with selected simulation time for different electrolytes: (g) $Mg(HMDS)_2$, (h) $Mg(HMDS)_2$ + OctylBr. (i) Raman spectra of DME solvent, $Mg(HMDS)_2$ salt, OctylBr additive, and different electrolytes.

The dynamic characteristics of Mg deposition are greatly influenced by the distributions of electric field and Mg^{2+} flux at the electrode-electrolyte interphase,[29-31] which can be studied by a finite element method (FEM) in COMSOL theoretical simulations. The 2D geometric models of Mg deposition in each electrolyte were first constructed based on the SEM results **(Figure S6)**. Due to a passivation-impeded, non-homogenous deposition in $Mg(HMDS)_2$

electrolyte, the electric field distribution is highly distorted, and the local current density tends to concentrate on the sharp edges of randomly existing dead Mg sites **(Figure 1c).**[32] This leads to the unfavorable tip effects through distorted distributions of Mg ion concentration alongside "hot spots" in the local electric field, further perturbing the non-uniform Mg^{2+} flux distribution **(Figure 1d)** and inducing the possibility of dendrite growth.[33] Introducing OctylBr into the electrolyte significantly homogenizes both the electric field (**Figure 1d)** and Mg^{2+} flux (**Figure 1f)** distributions by suppressing surface passivation and forming an SEI in situ that results in an even Mg deposition process. The evolution of the Mg^{2+} ion flux distribution at different time scales indicates anode passivation to occur rapidly in the $Mg(HMDS)_2$ electrolyte, as indicated by a reduced Mg^{2+} ion concentration at 0 s and further substantive decreases at 0.3 s and 0.6 s **(Figure 1g)**. In comparison, the planar Mg deposition from the $Mg(HMDS)_2$ + OcylBr electrolyte shows constant Mg^{2+} ion flux distribution near the electrolyte-electrode interface at all time scales **(Figure 1h)**.

To investigate the electrolyte structure and the influence of additives on solvation structure, we analyzed the Raman spectra of the DME solvent, $Mg(HMDS)_2$ salt, pure OctylBr additive, and different electrolytes **(Figure 1i)**. The pure $Mg(HMDS)_2$ salt exhibit peaks at 567 cm^{-1}, 617 cm^{-1}, and 671 cm^{-1}, corresponding to $MgHMDS^+$, 1D $\upsilon_{sym}Si{-}C$ (A_{1g}) and 2D $\upsilon_{sym}Si{-}C$ (E_g), respectively.[10, 34-36] Dissociation of $Mg(HMDS)_2$ salt into Mg^{2+} cation and $HMDS^-$ anion on dissolving in DME solvent is evidenced by the disappearance of $MgHMDS^+$ peak in Raman spectra of both $Mg(HMDS)_2$ and $Mg(HMDS)_2$ + OctylBr electrolytes.[34] Further, the redshift of $\upsilon_{sym}Si{-}C$ (A_{1g}) and 2D $\upsilon_{sym}Si{-}C$ (E_g) peaks in both the electrolytes strengthen the observation.[10] In contrast, the Raman spectrum of $Mg(HMDS)_2$ + $MgBr_2$ electrolyte retains the $MgHMDS^+$ peak, indicating poor salt dissociation. Additionally, a key peak at 869 cm^{-1}, attributed to solvent-separated Mg^{2+}-DME complexes (the major electroactive species), is present in the $Mg(HMDS)_2$ and $Mg(HMDS)_2$ + OctylBr electrolytes but absent in the

$Mg(HMDS)_2$ + $MgBr_2$ electrolyte. The Raman spectrum of pure OctylBr displays two characteristic peaks at 564 cm^{-1} and 646 cm^{-1}. Upon addition to $Mg(HMDS)_2$ electrolyte, these peaks undergo a red shift, confirming the presence of free OctylBr in the electrolyte. Notably, apart from these free OctylBr peaks, the remaining spectral features of the additive-modified electrolyte remain identical to those of the baseline $Mg(HMDS)_2$ electrolyte. This spectral consistency demonstrates that the fundamental solvation structure remains unaltered by OctylBr incorporation.

Along with suppressed anode passivation, the crystal structure and deposition morphology are also important in improving the cycling reversibility of Mg batteries.[31] The uneven deposition morphology and impure Mg deposition usually lead to rapid electrolyte depletion and hinder cycling performance. To elucidate crystal purity, we electroplated Mg into an Al substrate in an asymmetric cell and measured the electrodes retrieved with X-ray diffraction (XRD). The XRD pattern of the electrodeposited Mg in $Mg(HMDS)_2$ + OctylBr electrolyte **(Figure 2a top panel)** agrees closely with the P63/mmc space group of hexagonal Mg (JCPDS No. 35-0821), verifying the high purity of the electroplated Mg.[37] No Mg diffraction peaks were detected in the XRD pattern for the electrode retrieved from the cell cycled in $Mg(HMDS)_2$ electrolyte, in which only Al substrate peaks can be observed **(Figure 2a lower panel)**. These results were corroborated by the SEM images of the same electrodes, where uniform deposition of electrodeposited Mg in $Mg(HMDS)_2$ + OctylBr electrolyte can be seen all over the Al substrate, whereas only dead Mg sites were seen with the $Mg(HMDS)_2$ electrolyte **(Figure 2b)**. To ensure the high phase purity and to easily visualize the morphological evolution of Mg deposition in the $Mg(HMDS)_2$ + OctylBr electrolyte, electroplated Mg at extremely high areal capacity (25 mAh/cm^2) were studied with XRD and SEM. The XRD pattern of the electroplated Mg obtained agrees closely with a hexagonal Mg crystal structure (JCPDS No. 35-0821), indicating that the purity remains high even at an

extremely long deposition time of 50 hours **(Figure 2c)**. The SEM images provide evidence for the planar growth of Mg deposits in the $Mg(HMDS)_2$ + OctylBr electrolyte, in which the deposits are stacked well on the substrate surface and have a highly homogenous hexagonal morphology (**Figure 2d)**.

Based on the theoretical COMSOL simulations and experimental crystal structure analyses of electrodeposited Mg with and without the OctylBr additive, we determined the characteristics of initial Mg deposition (**Figure 2e-f**) as follows. In the $Mg(HMDS)_2$ electrolyte, the moisture content, and the anion reduction to the surface form an irreversible passivation layer on the anode surface, leading to the formation of many dead Mg sites. This eventually hinders the Mg^{2+} flux and electric field distributions, leading to a larger voltage drop and restricting Mg deposition **(Figure 2e)**. In the $Mg(HMDS)_2$ + OctylBr electrolyte, the passivation-free planar Mg deposition leads to the highly homogeneous electric field and Mg^{2+} flux distributions, enhancing the reversibility of the Mg deposition/dissolution **(Figure 2f)**.

2.2. Interfacial electrochemical kinetics

As interfacial electrochemical kinetics at the anode-electrolyte interface greatly influence the Mg plating/stripping process, we investigated this aspect with Tafel measurements and electrochemical impedance spectroscopy (EIS) using Mg//Mg symmetric cells **(Figure 2g-l)**. With the $Mg(HMDS)_2$ electrolyte, the Tafel plot reflected typical passivation characteristics, demonstrated by a plateau in a wider potential region.[38] With the $Mg(HMDS)_2$ + OctylBr electrolyte, a passivation-free Mg plating and stripping process is indicated by a drop in current at 0 V. The exchange current density (j_0) calculated from the Tafel curves commonly reveals the ion transport kinetics of the plating/stripping process.[39-40] The exchange current density for Mg plating/stripping in the $Mg(HMDS)_2$ + OctylBr electrolyte (158 $\mu A/cm^2$) is many times higher (**Figure 2h**) than that in the $Mg(HMDS)_2$ electrolyte (0.00859 $\mu A/cm^2$).

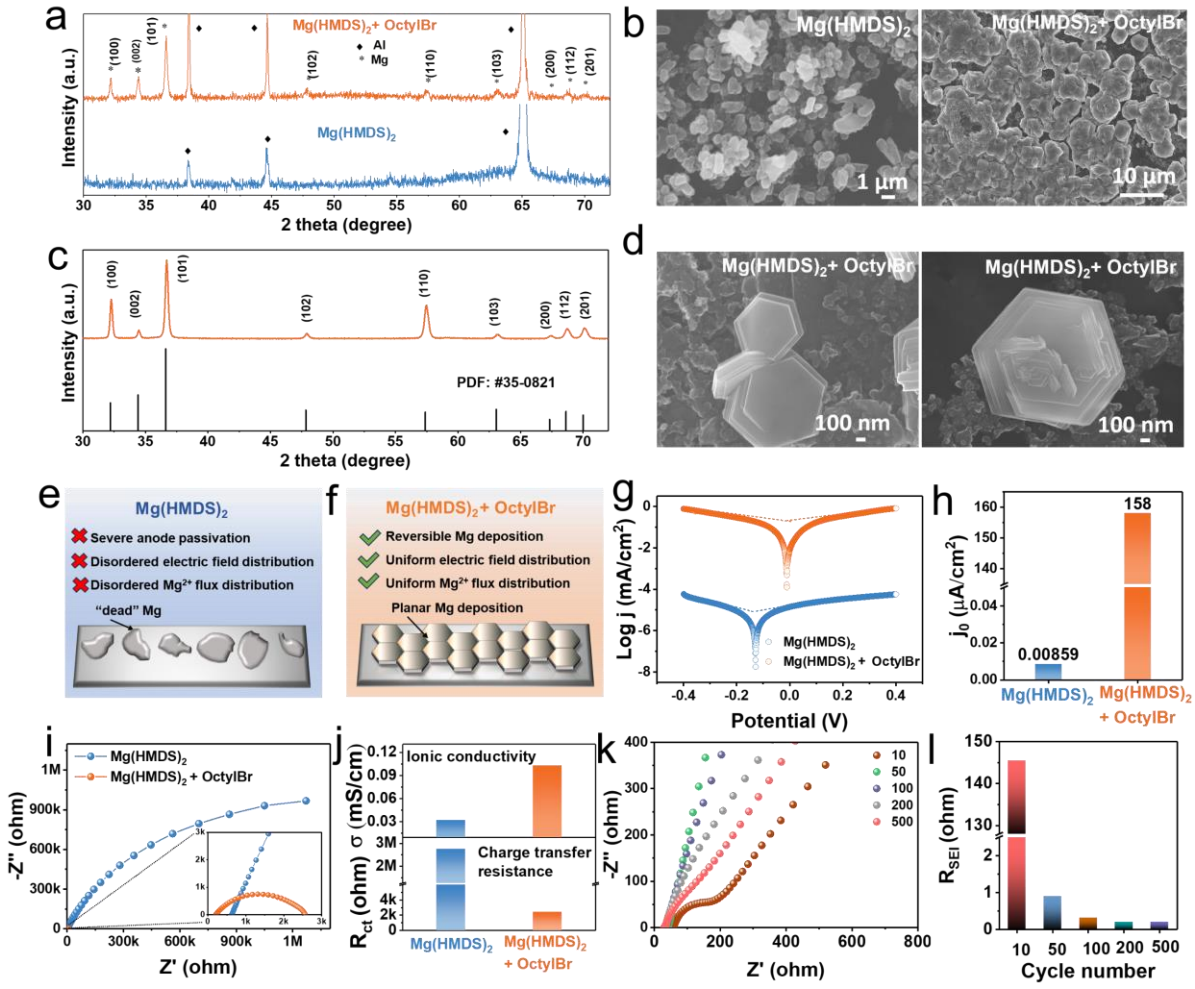

Figure 2. (a) XRD patterns of initial Mg deposits in different electrolytes; (b) SEM images of initial Mg plating in different electrolytes; (c) XRD pattern of Mg deposits in the $Mg(HMDS)_2$ + OctylBr electrolyte at 25 mAh/cm^2, 0.5 mA/cm^2; (d) SEM images of Mg deposits in the $Mg(HMDS)_2$ + OctylBr electrolyte at 25 mAh/cm^2, 0.5 mA/cm^2; (e-f) Schematic representation of Mg deposits and related effects from different electrolytes. Electrochemical kinetics studies at anode electrolyte interface in different electrolytes: (g) Tafel curves of symmetric Mg//Mg cells; (h) Measured exchange current from Tafel curves; (i) EIS Nyquist plot of Mg//Mg cells before cycling in different electrolytes; (j) Graphical representation of measured parameters from Nyquist plots in different electrolytes, (lower panel) R_{ct}, (upper panel) ionic conductivity; (k) EIS Nyquist curves of Mg//Mg cells in $Mg(HMDS)_2$ + OctylBr electrolyte at different cycles; (l) graphical representation of cycle number vs R_{SEI}.

The higher j_0 in the $Mg(HMDS)_2$ + OctylBr electrolyte indicates faster reaction kinetics at the microelectrode surface, suggesting that minimal overpotential is required to drive the electrochemical reaction.[40] The extremely low j_0 in $Mg(HMDS)_2$ electrolyte indicates the need for a larger overpotential to drive the Mg plating/stripping process as a result of a passivated surface. Subsequently, the electrolyte may not be able to 'refill' the consumed Mg^{2+} near the electrode surface, which leads to concentration gradient-induced Mg dendrite growth.[41] The EIS Nyquist plots of Mg//Mg symmetric cells in $Mg(HMDS)_2$ and $Mg(HMDS)_2$ + OctylBr electrolytes before cycling **(Figure 2i)** were fitted using the equivalent circuit (**Figure S7a**), which comprises a series resistance/electrolyte resistance (R_s), a charge transfer resistance (R_{ct}), and a constant phase element (CPE). In the $Mg(HMDS)_2$ electrolyte, an extremely high R_{ct} of 2.6×10^6 **Ω** justifies the anode passivation behavior observed in the studies described previously. Meanwhile, in the $Mg(HMDS)_2$ + OctylBr electrolyte, the R_{ct} decreases drastically to only 2428 **Ω**, indicative of a passivation-free anode surface and improved charge transfer kinetics at the interface (**Figure 2j (lower panel))**. Likewise, the R_s in the $Mg(HMDS)_2$ + OctylBr electrolyte (194.6 ohms) is also much lower than that of the $Mg(HMDS)_2$ electrolyte (624.3 ohms). The ionic conductivity (σ, mS/cm) of the electrolytes was calculated by Equation (1)

$$\sigma = \frac{L}{R_s \times S} \qquad (1)$$

where L represents the thickness of the separator (cm), S represents the contact area between the electrolyte and the electrode (cm^2), and R_s is the intrinsic series resistance/electrolyte resistance (Ω). The ionic conductivity (σ) of electrolytes measured by EIS (**Figure 2j**, **upper panel)**, is much higher in the $Mg(HMDS)_2$ + OctylBr (0.11 mS/cm) electrolyte than in the $Mg(HMDS)_2$ electrolyte (0.03 mS/cm). This confirms that introducing the OctyBr additive drastically improves the ionic mobility of the electrolyte.[37, 42] Since the $Mg(HMDS)_2$

electrolyte cannot undergo cycling, the EIS measurements after different cycles were only measured for the $Mg(HMDS)_2$ + OctylBr electrolyte. The Nyquist plots at different cycling states (0.5 mA/cm^2 and 0.5 mAh/cm^2, **Figure 2k**) changed from a single semicircle to two semicircles through a newly generated semicircle in the high-frequency region, proving the progression of SEI during cycling.[43-46] The curves obtained after cycling were obtained by using the equivalent circuit (**Figure S7b**), which comprises of additional resistance component (R_{SEI}) and constant phase element (CPE2).[42] The R_{SEI} indicates the resistance of Mg^{2+} migration through the SEI, and after 10 cycles it is only at 145.5 **Ω**, which reduces further to 0.905 **Ω** after just 50 cycles. This proves that a highly Mg^{2+} diffusive SEI is formed during cycling which enhances the Mg plating/stripping process (**Figure 2l)**.[37] Further cycling effectively promotes SEI progression and subsequently enhances the reversibility of Mg plating/stripping, which can be seen from the reduced R_{SEI} values after 100, 200, and 500 cycles (as low as 0.321 **Ω**, 0.211 **Ω**, and 0.205 **Ω** respectively).

2.3. Interfacial chemistry

We used time-of-flight secondary ion mass spectrometry (TOF-SIMS) and X-ray photoelectron spectroscopy (XPS) to elucidate the chemical composition of anode passivation in the $Mg(HMDS)_2$ electrolyte and the SEI formed in situ for the $Mg(HMDS)_2$ + OctylBr electrolyte. For both TOF-SIMS and XPS studies, the anode passivated in an Mg//Mg symmetric cell at the first cycle in $Mg(HMDS)_2$ electrolyte, and the anode retrieved from the Mg//Mg symmetric cell after 20 cycles (0.5 mA/cm^2, 0.5 mAh/cm^2) in the $Mg(HMDS)_2$ + OctylBr electrolyte were used. The 3D-rendered TOF-SIMS images (**Figure 3a-b**) helped us understand the three-dimensional distribution of the different interfacial species. The high intensity of the MgO^- fragments observed on the surface of the anode in $Mg(HMDS)_2$ **(Figure 3b)** easily explains the surface passivation of the anode by the native oxide, which also confirms the impediment to Mg deposition observed from the SEM and XRD studies. The distribution of $C_2H_3O^-$

fragments in bulk is ascribed to the presence of electrolyte decomposition products on the anode. Notably, no Br^- and $MgBr^-$ species were found in the anode passivated in the $Mg(HMDS)_2$ electrolyte, and weaker C^- fragments indicate the absence of desirable organic-rich surfaces. Meanwhile, the anode retrieved from the cycled cell in the $Mg(HMDS)_2$ + OctylBr electrolyte **(Figure 3a)** displays a passivation-free surface as evidenced by the weaker MgO^- fragments on it. The anode is predominantly enriched with Br-based species (Br^- and $MgBr^-$), confirming the effective formation of Br-rich SEI during cycling. The decomposition product ($C_2H_3O^-$) signal is notably weaker and limited only to the surface; this is the result of effective anode protection through a robust Br-rich SEI formed in situ. The strong signals from the C^- fragments on the surface prove the formation of an organic-rich surface and the presence of Si^- fragments beneath the surface also can be considered part of inorganic SEI. The intensity vs etching depth graph obtained from TOF-SIMS analysis (**Figure 3c-d**) shows that the MgO^- peak intensity in the $Mg(HMDS)_2$ electrolyte is extremely high, which is indicative of Mg anode passivation by native oxides, and the flattened peak for Br^- is evidence for the absence of the SEI. In the $Mg(HMDS)_2$ + OctylBr electrolyte, the high Br^- signals the in-situ formation of a Br-rich SEI, and the flatter MgO^- peak intensity confirms passivation suppression.

Evidence from the surface XPS spectra (**Figure 3e-h**) further supports the observations from TOF-SIMS and helps determine the chemical composition of interface species. The C 1s spectrum **(Figure 3e)** of the anode in $Mg(HMDS)_2$ electrolyte shows a strong intensity of C-C peaks at 284.5 eV, and less intense peaks at 286.3 eV, 288.2 eV, and 289.5 eV, corresponding to C-O, C=O, and $C_2O_4^{2-}/CO_3^{2-}$ respectively, which all originate mainly from the decomposition of the DME solvent.[9, 46-48] Conversely the surface C 1s spectrum of the anodes cycled in $Mg(HMDS)_2$ + OctylBr shows relatively less intense C-C, C=O, and $C_2O_4^{2-}/CO_3^{2-}$ peaks, and is missing a C-O peak, which verifies the paucity of solvent decomposition products on the anode surface. Instead, a strong peak can be indexed at 285.6 eV, which is attributed to

the C-O-C signal of the ether functional group from polyether. Ethereal species have been proven to have superior compatibility with Mg metal anodes, effectively protecting the anode surface from passivation and solvent/electrolyte decomposition.[9, 49] The results from surface O 1s spectra **(Figure 3f)** further confirm that only the anode cycled in the $Mg(HMDS)_2$ + OctylBr electrolyte exhibits the peak that corresponds to the ether functional group (C-O-C) at 532.4 eV.[34] In comparison, the passivated anode in the $Mg(HMDS)_2$ electrolyte shows a high concentration of solvent decomposition species (C-O/C=O) at 531.3 eV.[43]

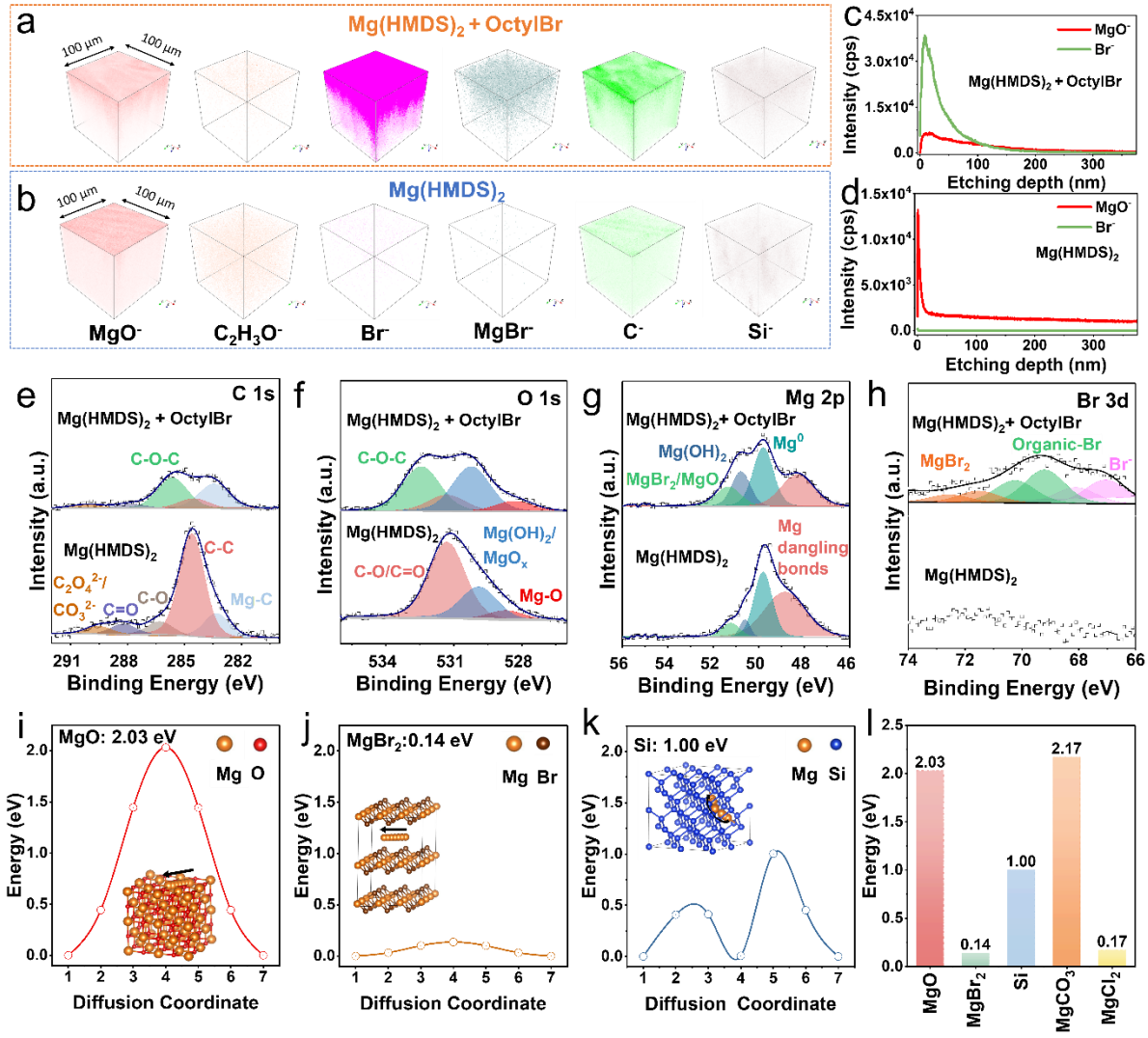

Figure 3. Chemical and elemental composition studies of passivated anode in $Mg(HMDS)_2$ electrolyte and cycled anode in $Mg(HMDS)_2$ + OctylBr electrolyte: (a-b) 3D-rendered TOF-SIMS images; (c-d) Intensity evolution of MgO^- and Br^- species as a function of etching depth;

(e-h) Surface XPS composition analysis; (i-k) Calculated Mg migration barrier in bulk MgO, $MgBr_2$, and Si; (l) Graphical comparison of Mg migration barrier values in different passivating native oxide layers and SEI components.

The peaks in the Mg 2p spectra **(Figure 3g)** can be deconvoluted into Mg^0 (49.8 eV), $Mg(OH)_2$ (50.6 eV), $MgBr_2$/MgO (51.3 eV), and Mg dangling bonds (48.3-48.8 eV).[24] The passivated Mg anode in the $Mg(HMDS)_2$ electrolyte has substantially fewer inorganic SEI components ($Mg(OH)_2$ and $MgBr_2$) than the anodes cycled in the $Mg(HMDS)_2$ + OctylBr electrolyte. Since both the $MgBr_2$ and MgO species have the same peak position in the Mg 2p spectra, it is hard to discern the contribution of each component. However, a flat Br 3d spectrum in the $Mg(HMDS)_2$ electrolyte confirms the absence of $MgBr_2$ species, rendering the $MgBr_2$/MgO peak in Mg 2p only attributable to MgO **(Figure 3h)**. Three doublet peaks related to Br^-, organic-Br, and $MgBr_2$ species can be seen in Br 3d spectra of the anode cycled in the $Mg(HMDS)_2$ + OctylBr electrolyte. This strongly confirms the formation of a bromine-rich SEI during cycling. The Si 2p peaks indicate the existence of metallic Si and residual Si-C, which result from the reduction of $HMDS^-$ anions at the Mg metal surface **(Figure S8)**. Metallic silicon can protect an anode from passivation by being an interim SEI component.[10] The combined results of the XPS and TOF-SIMS studies indicate that the SEI formed in the $Mg(HMDS)_2$ + OctylBr electrolyte is of a hybrid nature, with an organic-rich surface and a robust inorganic layer beneath it. The organic-rich surface can provide mechanical stability to the SEI and prevent it from cracking during cycling, while the inorganic layer provides high Mg^{2+} ion conductivity.[17, 50-51] Moreover, the passivated anode in $Mg(HMDS)_2$ electrolyte, majorly comprises native oxide with a considerable amount of electrolyte/solvent decomposition products. We used density functional theory (DFT) calculations to understand the Mg diffusion mechanism in the different anode-electrolyte interphase species **(Figure 3i-k)**. The calculated diffusion energy barrier of the Mg atoms on $MgBr_2$ is 0.14 eV, which is

substantially lower than those of either the passivating MgO (2.03 eV) present in the $Mg(HMDS)_2$ electrolyte or of other reported SEI layers such as $MgCO_3$ (2.17 eV).[30] The Mg ion diffusion barrier in $MgBr_2$ is superior to that of the $MgCl_2$-based (0.17 eV) SEI component **(Figure 3l)**.[30]

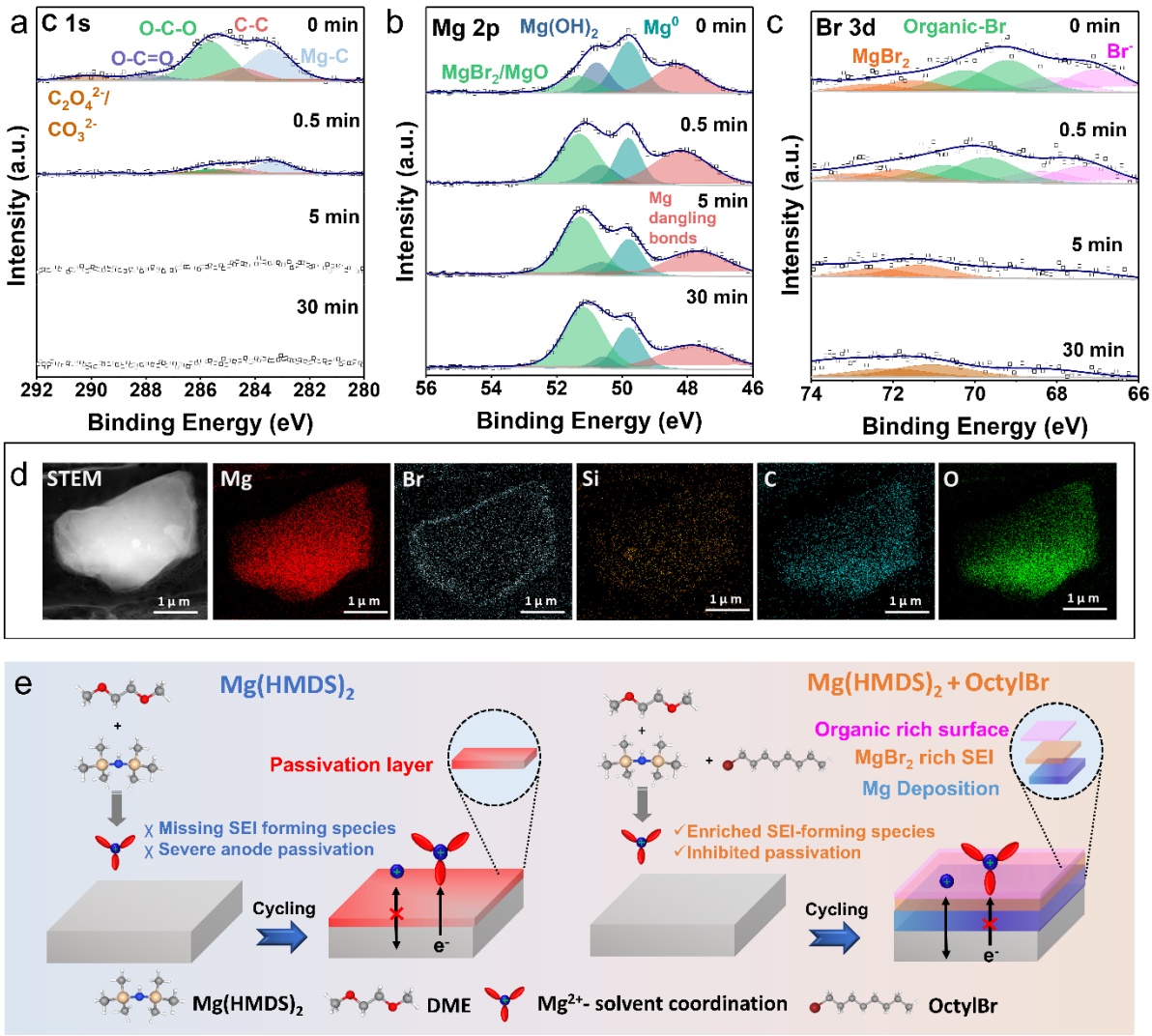

Figure 4. (a-c) Depth profiling XPS spectra of cycled Mg anode in the $Mg(HMDS)_2$ + OctylBr electrolyte: (a) C 1s, (b) Mg 2p, (c) Br 3d; (d) Cryo-STEM images and the corresponding EDS mapping of Mg deposits in the $Mg(HMDS)_2$ + OctylBr electrolyte; (e) Schematic illustrations showing the evolution of electrode-electrolyte interphases in $Mg(HMDS)_2$ and $Mg(HMDS)_2$ + OctylBr electrolytes.

To further understand the chemical composition of the in-situ formed SEI layer in the $Mg(HMDS)_2$ + OctylBr electrolyte, we conducted depth profiling XPS analysis of the cycled anodes at different etching times of 0, 0.5, 5, and 30 min of Ar etching. The C 1s **(Figure 4a)** and O 1s **(Figure S9a)** spectra at different etching times indicate that the surface is enriched with higher organic ethereal compounds (C-O-C), which substantially decreases at an etching time of 0.5 min and completely disappears at longer etching times. A protective organic layer is necessary to protect the electrode from electrolyte degradation and improve the reversibility of Mg deposition.[10] The deconvoluted Mg 2p spectra **(Figure 4b)** at different etching times reveal that $MgBr_2$ is the key inorganic SEI species. This is further confirmed by the Br 3d spectra **(Figure 4c)**. Even though the surface is dominated by organic-Br and adsorbed Br^- species, both the species completely diminished with an etching time of only 0.5 min, and the deeper SEI layer is largely comprised of $MgBr_2$ species in agreement with observations from the TOF-SIMS analysis. In the Si 2p spectra **(Figure S9b),** metallic Si can be seen at all etching depths. Their presence is the result of the reduction of $HMDS^-$ and they are thought to be part of the inorganic SEI.[24]

Cryogenic electron microscopy (cryo-EM), an emergent imaging technology renowned for the structural elucidation of biomaterials, recently offers increased possibilities for analyzing sensitive battery materials.[52-54] The Cryo-STEM and corresponding EDS images of the Mg deposit not only indicate a planar structural morphology that is regulated from the $Mg(HMDS)_2$ + OctylBr electrolyte but also help us directly visualize the Br-rich SEI **(Figure 4d)**. The EDS images obtained from Cryo-STEM are a clear representation of this SEI which contains high concentrations of Br at the edges of the electrodeposited Mg, but not any other atomic species. However, the Cryo-STEM images of Mg deposits from $Mg(HMDS)_2$ **(Figure S10)** only indicate agglomerated Mg particles, indication of numerous “dead Mg” which

restrict the Mg plating. Further the EDS images reveal that the surface possesses higher oxygen content, which is attributed to surface passivation of anode by MgO species.

From the results of our studies on the interface chemistry, we propose the mechanisms associated with anode passivation in the $Mg(HMDS)_2$ electrolyte and SEI development in the $Mg(HMDS)_2$ + OctylBr electrolyte (**Figure 4e).** In the $Mg(HMDS)_2$ electrolyte, the Mg salt dissolves and forms the Mg^{2+}-solvent coordinate with DME, leaving the electrolyte without any SEI-forming species. Due to solvent decomposition and moisture attack on the anode surface, irreversible anode passivation is inevitable. The addition of OctylBr additive enriches the electrolyte with Br-based SEI forming species. The more rapid reaction kinetics between Mg anode and OctylBr produce an SEI formed in situ from the very initial cycle, whose subsequent growth is enhanced through further cycling. The SEI thus formed is of a hybrid nature, having an organic-rich surface and an $MgBr_2$-rich inorganic layer. It inhibits anode passivation and drastically improves cycling.

2.4. Electrochemical performance of $Mg(HMDS)_2$ + OctylBr electrolyte.

Understating the long-term cycling stability and voltage polarization of the Mg plating/stripping process is necessary for developing an effective Mg electrolyte, which was demonstrated by galvanostatic cycling in symmetric Mg//Mg cells **(Figure 5a)**.[48, 55-57] Due to predicted severe anode passivation in the $Mg(HMDS)_2$ electrolyte, the initial voltage hysteresis of the cell was undesirably high at 3.2 V, followed by rapid short-circuiting and the loss of cycling ability.[38, 58-59] By contrast, the $Mg(HMDS)_2$ + OctylBr electrolyte exhibited high Mg plating/stripping reversibility, which was confirmed by a cycling life of 3600 hours at 0.5 mA/cm^2 and 0.5 mAh/cm^2. The voltage profile at different time stamps of the Mg plating/stripping process **(Figure 5a-insets)** indicates that voltage hysteresis is ± 175 mV in

the earlier cycles that progressively reduced to ± 75 mV after 500 cycles. This is attributed to the apparent activation process in the initial stage.[47]

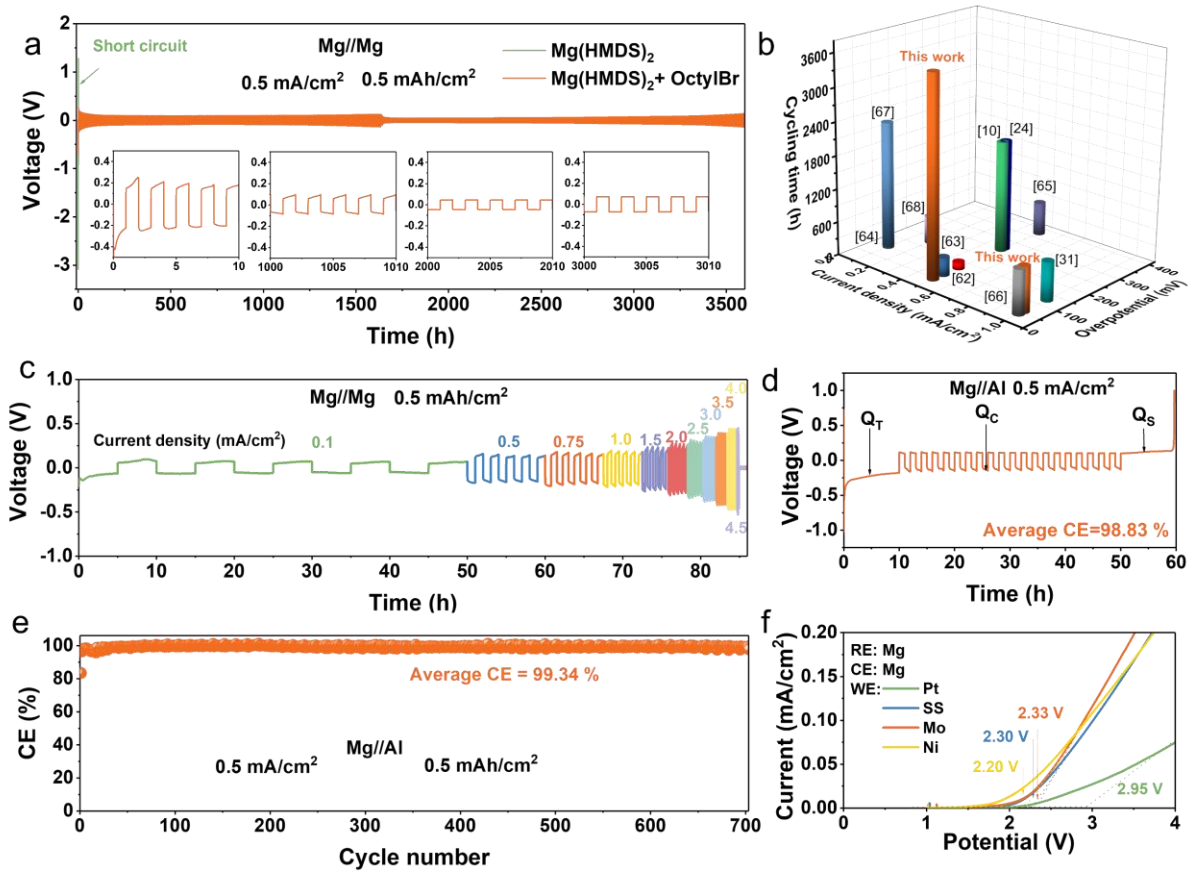

Figure 5. (a) Galvanostatic cycling profiles of Mg//Mg symmetric cells in $Mg(HMDS)_2$ and $Mg(HMDS)_2$ + OctylBr electrolytes (insets: different time stamps of voltage profile in $Mg(HMDS)_2$ + OctylBr electrolyte); (b) Comparison of $Mg(HMDS)_2$ + OctylBr electrolyte performance with previously reported $Mg(HMDS)_2$ based Mg battery electrolytes in terms of cycling life and overpotential; (c) Galvanostatic cyclic profiles of Mg//Mg symmetric cells in the $Mg(HMDS)_2$ + OctylBr electrolyte at different applied current; (d) Galvanostatic cyclic profile of the Mg//Al asymmetric cell during Aurbach tests with the $Mg(HMDS)_2$ + OctylBr electrolyte; (e) Cycle number vs CE of Mg//Al cell in the $Mg(HMDS)_2$ + OctylBr electrolyte during long term cycling test; (f) Linear sweep voltammetry curves with different metals as working electrodes in the $Mg(HMDS)_2$ + OctylBr electrolyte.

The slight voltage drop observed after 1600 h of cycling likely stems from negligible noise in the voltage profiles of few cycles (from 813-818 cycles), suggesting a transient soft short circuit **(Figure S11)**. However, subsequent cycles exhibit no abrupt voltage decline, and prolonged cycling reveals no evidence of this soft short escalating into a hard short circuit, a scenario that would typically manifest as severe overpotential or flat voltage profile. Notably, the cell immediately recovers its stability and continues cycling for over 1800 cycles without degradation. This rapid recovery is attributed to free OctylBr additives present in the electrolyte as evidenced from Raman analysis of electrolytes, which dynamically repair and reinforce the SEI layer during cycling. Due to the promotion of the Mg plating/stripping process during cycling by reinforced SEI, a lower voltage hysteresis of ± 45 mV can be achieved after about 1000 cycles, which is attributed to the enhanced Mg^{2+} mobility through the SEI, and confirmed by the EIS measured at different cycles **(Figure 2l)**.[60-61] The gradual increase in voltage hysteresis only at a very long cycling time of about 3600 h (1800 cycles) is due to slight electrolyte loss/decomposition as a result of prolonged cycling.[9] The flatter curves at all the cycling states indicate Mg deposition to be highly homogenous as a result of planar Mg deposition and an SEI established in situ. The electrolyte continued to show a commendable cycling life of 804 hours with a voltage hysteresis of only ± 55 mV even when the cycling conditions were doubled to 1 mA/cm^2 and 1 mAh/cm^2 **(Figure S12b)**. The cycling life and overpotential performance of the $Mg(HMDS)_2$ + OctylBr electrolyte in symmetric cells outperformed the previously reported electrolytes based on $Mg(HMDS)_2$ salt (**Figure 5b** and **Table S1)**.[10, 24, 31, 62-68] Furthermore, compared with the best performing Mg electrolytes, the cycling life and overpotential of the $Mg(HMDS)_2$ + OctylBr in symmetric cells is better than most of them in the literature based on different Mg salts (**Table S2)**.[2, 29, 47-48, 55, 57, 61, 69-73]

The high current densities applied during cycling typically increase the possibility of dendrite formation and deter the reversibility of Mg plating/stripping.[31, 74] Interestingly, the

$Mg(HMDS)_2$ + OctylBr electrolyte performed exceptionally in the multi-current rate test conducted in Mg//Mg symmetric cells **(Figure 5c)** with a high limiting current of 4.5 mA/cm^2, surpassing the performances reported for most of the best-performing electrolytes that show limiting currents of less than 2 mA/cm^2**.**[10, 37-38, 44, 47, 49, 57-58, 60] Despite showing increasing overpotential with increasing applied current density, the voltage profiles remain flat, indicating that the electrolytes allowed homogenous Mg deposition even at high current densities **(Figure S13a)**. Even at an elevated applied current of 4.0 mA/cm^2, the $Mg(HMDS)_2$ + OctylBr electrolyte demonstrated a much lower voltage hysteresis of only ± 400 mV **(Figure S13b)**. To examine the reversibility and real-time coulombic efficiency (CE) of the Mg plating/stripping process, we evaluated the Mg//Al asymmetry cell using the Aurbach CE test.[48, 75] A Mg reservoir (Q_T= 5 mAh/cm^2) was deposited on the Al/C cathode at a current density of 0.5 mA/cm^2 (**Figure 5d**), after which the cell was cycled at 0.5 mA/cm^2 and 0.5 mAh/cm^2 (Q_C) for 20 cycles, and the electroplated Mg was stripped with a cutoff potential of 1V (Q_S). The average CE is calculated by Equation (2)

$$CE_{Avg} = (20Q_C + Q_S)/(20Q_C + Q_T) \quad (2)$$

The $Mg(HMDS)_2$ + OctylBr electrolyte showed a remarkable average CE of 98.83%, highlighting excellent Mg reversibility due to planar Mg deposition even at high areal capacities and the ready formation of SEI during the early cycles. To ascertain the long-term cycling stability in asymmetric cells, we tested the $Mg(HMDS)_2$ + OctylBr electrolyte in Mg//Al cell at 0.5 mA/cm^2 and 0.5 mAh/cm^2, which resulted in an average CE of 99.34% with a cycling life of 703 cycles with a minimal Mg plating/stripping overpotential of only 0.22 V **(Figure 5e and Figure S14)**. We subjected the $Mg(HMDS)_2$ + OctylBr electrolyte to linear sweep voltammetry (LSV) in a three-electrode flooded cell **(Figure 5f)** to understand its anodic stability window. We found our electrolyte to achieve reasonable anodic stability with different

non-noble metals as working electrodes [2.20 V (Ni), 2.30 V (SS), and 2.33 V (Mo)], markedly superior to the organic chloride-modified analogue ($Mg(HMDS)_2$ + OctylCl) which showed lower stability at 1.79 V (Ni), 1.97 V (SS), and 1.75 V (Mo) **(Figure S15)**. Both electrolytes exhibited almost similar anodic stability with inert Pt electrode (2.95 V for $Mg(HMDS)_2$ + OctylBr and 2.97 V for $Mg(HMDS)_2$ + OctylCl). Furthermore, the comparison **(Table S3)** of LSV onset potential reveals that our electrolytes are comparable to or only slightly lower than reported Cl/Br additive modified commercial salt-based electrolytes. Since the LSV curves only allows rapid testing, the chronoamperometric profiles **(Figure S16)** were recorded on both Pt and non-noble metal electrodes to understand the oxidation stability and corrosion behavior of our electrolyte.[10] Crucially, the absence of abrupt current surges during prolonged polarization at fixed potentials confirms robust resistance against electrolyte oxidative decomposition and/or metal electrode corrosion. This is further corroborated by post-mortem SEM analysis of metals after chronoamperometry tests **(Figure S17)**, which reveals pristine electrode surfaces without morphological degradation, a critical indicator of the electrolyte compatibility with practical current collectors.

Generally, the constrained areal capacities of Mg anodes (0.02-1 mAh/cm^2) in traditional electrolytes due to inhomogeneous distributions of electric field and Mg^{2+} flux from uneven Mg deposition hampers the practical applicability of RMBs.[12-16] However, owing to planar deposition that results in highly homogenous electric fields and Mg^{2+} flux distributions, the $Mg(HMDS)_2$ + OctylBr electrolyte performed very commendably in a stepwise incremental capacity test both in symmetric (**Figure 6a**) and asymmetric cells **(Figure S18),** which showed reversible cycling up to 20 mAh/cm^2 at 0.5 mA/cm^2. Encouragingly, our electrolyte performs consistently at all areal capacities, as demonstrated by flatter voltage profiles that ensure highly homogeneous Mg deposition **(Figure S19)**. The high average CE values (96.39-99.25%) in asymmetric cells ensure excellent reversibility even at high areal capacities (**Figure 6b**). The

standalone cycling stability of the $Mg(HMDS)_2$ + OctylBr electrolyte under different areal capacity (1, 2, 5 10, 20 and 25 mAh/cm^2) was also assessed by galvanostatic cycling at 0.5 mA/cm^2 (**Figure 6c-d and Figure S20)**. Even at such high areal capacities, the electrolyte demonstrated a superior cycling life with low overpotentials. For instance, the Mg//Mg symmetric cells at higher areal capacities of 5 mAh/cm^2 (**Figure 6c**) and 10 mAh/cm^2 (**Figure 6d**), the electrolyte achieved a cycling life of 820 hours and 640 hours, respectively. In asymmetric cells, the electrolyte demonstrated promising CE values at all tested areal capacities, at 1 mAh/cm^2 the CE is 99.46%, with 25-fold increase of areal capacity, the CE remains as high as 98.10% for 25 mAh/cm^2 (**Figure 6e**). Notably, the flatter voltage profiles obtained in symmetric **(Figure S21)** and asymmetric cells **(Figure 6f)** at different areal capacities proves the effectiveness of the $Mg(HMDS)_2$ + OctylBr electrolyte in allowing for homogeneous planar Mg deposition with a minimal voltage hysteresis to drive electrochemical reactions.

2.5. Full cell testing

To determine the capability of the $Mg(HMDS)_2$ + OctylBr electrolyte in practical applications, we studied the performance of full cells assembled with a Mo_6S_8 cathode. The CV curve obtained with the $Mg(HMDS)_2$ electrolyte is flat, indicating anode passivation that limits cycling in the cell **(Figure 6g).** A well-defined pair of anodic and cathodic peaks are observed with the $Mg(HMDS)_2$ + OctylBr electrolyte that correspond to the intercalation and deintercalation of divalent Mg^{2+} ions respectively. The initial discharge and charge capacities with the $Mg(HMDS)_2$ + OctylBr electrolyte are 77.88 mAh/g and 71.85 mAh/g respectively. The polarization voltage (ΔE), which is the potential difference at 50% of the charge and discharge capacities, is only 0.70 V **(Figure S22a).** The cycle number vs discharge capacity and coulombic efficiency curves indicate that the full cell can cycle for up to 70 cycles with an average CE of 99.15 % at 0.1 C **(Figure 6h)**. Rate capability tests conducted showed that the

cells can cycle at up to 0.2 C, verifying electrolyte effectiveness under full-cell testing **(Figure 6i and Figure S22b).**

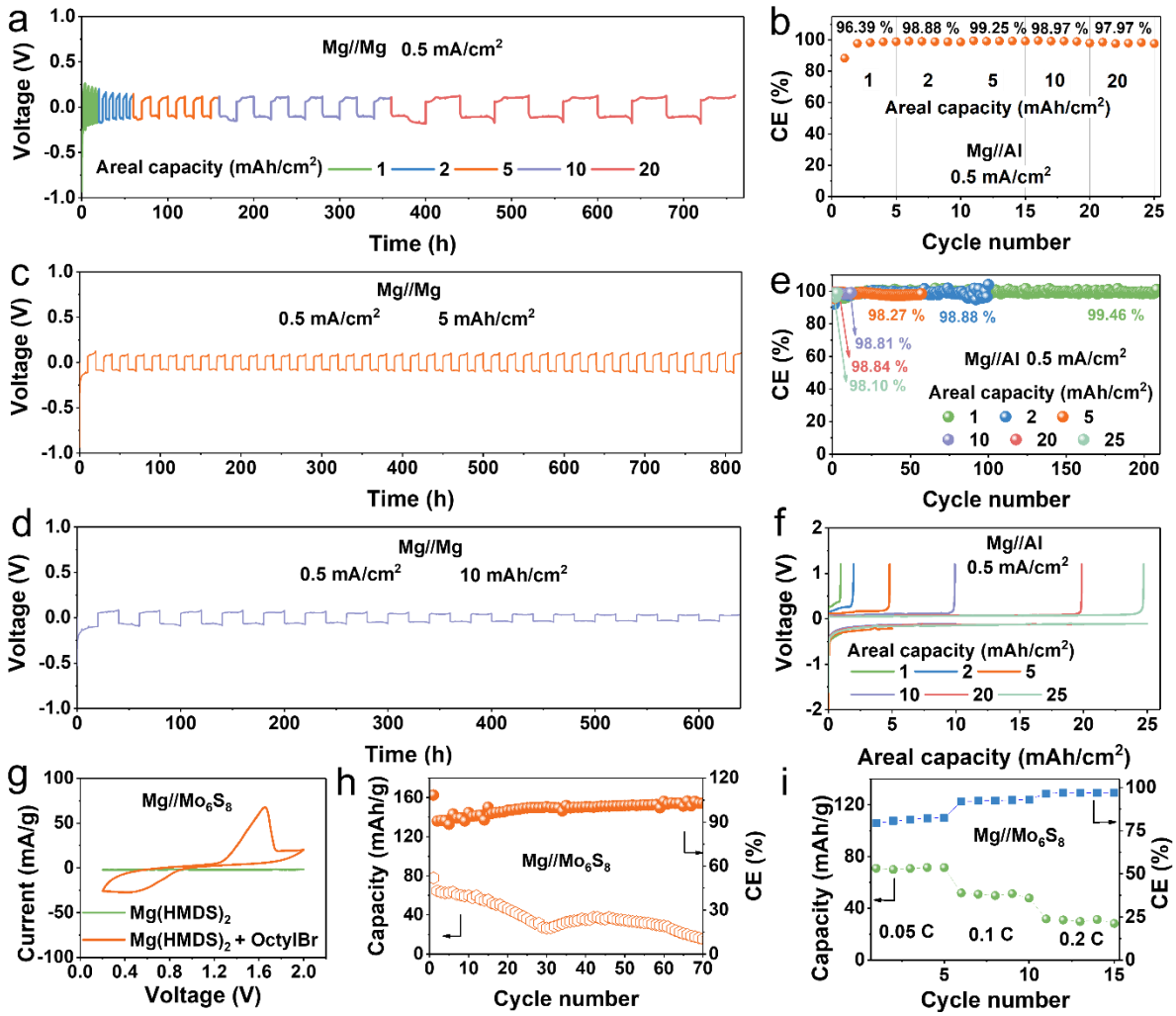

Figure 6. Electrochemical performance of the $Mg(HMDS)_2$ + OctylBr electrolyte: (a) Cycling profile of Mg//Mg cell measured at stepwise incremental areal capacities; (b) Cycle number vs CE graph of Mg//Al cell measured at stepwise incremental areal capacities; (c) Galvanostatic cycling profile of the Mg//Mg cell at 5 mAh/cm^2 (0.5 mA/cm^2); (d) Galvanostatic cycling profile of the Mg//Mg cell at 10 mAh/cm^2 (0.5 mA/cm^2); (e) Cycle number vs coulombic efficiency plot of Mg//Al cells measured at different areal capacities. (f) First cycle Voltage profile of Mg//Al cells at different areal capacities in $Mg(HMDS)_2$ + OctylBr electrolyte at 0.5 mA/cm^2. Electrochemical performance of full cell testing with Mo_6S_8 cathode: (g) Cyclic

voltammetry curves at a scan rate of 10 mV s^{-1}; (h) Cycle number vs discharge capacity and coulombic efficiency measured at 0.1 C; (i) Cycle number vs discharge capacity and coulombic efficiency at different C rates.

2.6. Future potential of OctylBr as an additive in Mg electrolytes

To ensure the effectiveness of the OctylBr additive in improving the reversibility of other passivating Mg salts, we tested it with electrolytes formulated with magnesium triflate ($Mg(OTf)_2$) and magnesium bis-(trifluoromethanesulfonimide) ($Mg(TFSI)_2$) salts. In symmetric Mg/Mg cells, $Mg(OTf)_2$ + OctylBr and $Mg(TFSI)_2$ + OctylBr electrolytes were found to cycle for up to 827 hours and 155 hours respectively, at 0.5 mA/cm^2 and 0.5 mAh/cm^2 **(Figure S23).** The asymmetric Mg//Al cells **(Figure S24a)** tested were found to cycle for up to 270 cycles and 70 cycles in $Mg(OTf)_2$ + OctylBr and $Mg(TFSI)_2$ + OctylBr electrolytes, respectively, with average CEs of 98.52% and 93.50%. The Mg plating/stripping overpotential in the asymmetric cells are as low as 0.27 V ($Mg(OTf)_2$ + OctylBr) and 0.18 V ($Mg(TFSI)_2$ + OctylBr), indicating a regulated deposition morphology and a robust SEI that enables passivation-free Mg deposition/dissolution **(Figure S24b-c)**. The SEM images **(Figure S25a)** and XRD patterns **(Figure S25b)** of initial deposits in different OctylBr-modified conventional electrolytes indicate the occurrence of very similar Mg deposition and phase pure hexagonal Mg crystal structure (PDF No: 35-0821) irrespective of the Mg salt used. We further determined the elemental composition of SEI formed in each of the systems by studying the cycled anodes in the corresponding electrolytes. The 3D rendered TOF-SIMS images of the cycled anodes suggest suppressed anode passivation in all cases, as indicated by fewer MgO^- fragments on the anode surface **(Figure S26)**. Moreover, Br-rich SEIs were observed to form in situ for all electrolyte systems, along with highly reduced electrolyte degradation products ($C_2H_3O^-$ and $CF_3SO_3^-$). The shorter cycling life observed with the $Mg(TFSI)_2$ + OctylBr and $Mg(OTf)_2$ + OctylBr electrolytes may be due to thicker SEI formation and

interference from the MgF_2-based SEI component that typically possesses poor Mg^{2+} migration properties. Further, the surface XPS F 1s spectra comparison **(Figure S27a)** of anodes cycled in $Mg(TFSI)_2$ + OctylBr and $Mg(OTf)_2$ + OctylBr electrolytes corroborates these findings. Notably, the $Mg(TFSI)_2$ + OctylBr electrolyte system exhibits significantly higher MgF_2 content throughout the SEI layer, as evidenced by depth-profiling XPS analysis **(Figures S27b-c).** This pronounced presence of MgF_2 in SEI layer with poor ionic conductivity directly correlates with the inferior cycling stability of $Mg(TFSI)_2$ + OctylBr compared to the other electrolyte formulations studied. The surface XPS comparison of anodes reveals cycling life to be directly proportional to the amount of ethereal O-C-O components, which can be visualized by the C 1s and O 1s spectrum **(Figure S28a-b)**. This strongly confirms the importance of achieving an organic-rich SEI surface. Raman spectroscopic analysis of conventional Mg salt-based electrolytes reveals that the incorporation of OctylBr additive preserves both the solvation structure and electroactive species, regardless of the electrolyte anion composition **(Figure S29)**. The commendable performance enhancement conferred by the OctylBr additive to conventional passivating electrolytes indicates its adaptability and opens new avenues for future investigation.

3. Conclusion

In summary, we introduced a multifunctional OctylBr additive to the heavily passivating traditional $Mg(HMDS)_2$ electrolyte to improve the reversibility of Mg plating/stripping by regulating the SEI and Mg deposition morphology. The additive offered several advantages including (i) suppressed Mg anode passivation, (ii) improved surface electrochemical kinetics, (iii) planar deposition with uniform morphology, and (iv) formation of Br-rich anode-electrolyte interphase in situ. The modified electrolyte significantly extended the cycling life from 0 hours to nearly 3600 hours in symmetric cells and a higher CE of 99.34% in asymmetric cell at 0.5 mA/cm² and 0.5 mAh/cm². Due to the planar deposition morphology, the electrolyte

demonstrated reversible Mg plating and stripping even at high areal capacities of up to 25 mAh/cm². Significant cycling times of 820 hours and 640 hours were achieved at higher operational areal capacities of 5 mAh/cm² and 10 mAh/cm², respectively, in symmetric cells, underscoring the effectiveness of the electrolyte for high-energy applications. Furthermore, full cell cycling with Mo_6S_8 cathode and the superior generalized performance of the OctylBr additive with other conventional Mg salts indicate the effectiveness of the electrolyte additive in increasing RMB performance. Our study highlights the importance of regulating both deposition morphology and SEI via organic bromine additives for highly reversible Mg anode with superior areal capacity and ultralow voltage hysteresis.

Supporting Information

Supporting Information is available from the Wiley Online Library or from the author.

Acknowledgements

Z.W.S. was supported by the Singapore National Research Foundation (NRF Investigatorship NRF-NRFI09-0002) and the Agency for Science, Technology and Research (MTC Programmatic Fund M23L9b0052).

Conflict of Interest

The authors declare no conflict of interest.

References

1. Muldoon, J.; Bucur, C. B.; Gregory, T., Quest for Nonaqueous Multivalent Secondary Batteries: Magnesium and Beyond. *Chemical Reviews* **2014**, *114*, 11683-11720.

2. Tang, K.; Du, A.; Dong, S.; Cui, Z.; Liu, X.; Lu, C.; Zhao, J., et al., A Stable Solid Electrolyte Interphase for Magnesium Metal Anode Evolved from a Bulky Anion Lithium Salt. *Advanced Materials* **2020**, *32*, 1904987.

3. Son, S.-B.; Gao, T.; Harvey, S. P.; Steirer, K. X.; Stokes, A.; Norman, A.; Wang, C., et al., An Artificial Interphase Enables Reversible Magnesium Chemistry in Carbonate Electrolytes. *Nature Chemistry* **2018**, *10*, 532-539.

4. Lv, R.; Guan, X.; Zhang, J.; Xia, Y.; Luo, J., Enabling Mg Metal Anodes Rechargeable in Conventional Electrolytes by Fast Ionic Transport Interphase. *National Science Review* **2019**, *7*, 333-341.

5. Li, B.; Masse, R.; Liu, C.; Hu, Y.; Li, W.; Zhang, G.; Cao, G., Kinetic Surface Control for Improved Magnesium-Electrolyte Interfaces for Magnesium Ion Batteries. *Energy Storage Materials* **2019**, *22*, 96-104.

6. Wei, C.; Tan, L.; Zhang, Y.; Xi, B.; Xiong, S.; Feng, J.; Qian, Y., Highly Reversible Mg Metal Anodes Enabled by Interfacial Liquid Metal Engineering for High-Energy Mg-S Batteries. *Energy Storage Materials* **2022**, *48*, 447-457.

7. Hou, S.; Ji, X.; Gaskell, K.; Wang, P.-f.; Wang, L.; Xu, J.; Sun, R., et al., Solvation Sheath Reorganization Enables Divalent Metal Batteries with Fast Interfacial Charge Transfer Kinetics. *Science* **2021**, *374*, 172-178.

8. Wang, H.; Feng, X.; Chen, Y.; Liu, Y.-S.; Han, K. S.; Zhou, M.; Engelhard, M. H., et al., Reversible Electrochemical Interface of Mg Metal and Conventional Electrolyte Enabled by Intermediate Adsorption. *ACS Energy Letters* **2020**, *5*, 200-206.

9. Nguyen, D.-T.; Eng, A. Y. S.; Horia, R.; Sofer, Z.; Handoko, A. D.; Ng, M.-F.; Seh, Z. W., Rechargeable Magnesium Batteries Enabled by Conventional Electrolytes with Multifunctional Organic Chloride Additives. *Energy Storage Materials* **2022**, *45*, 1120-1132.

10. Horia, R.; Nguyen, D.-T.; Eng, A. Y. S.; Seh, Z. W., Using a Chloride-Free Magnesium Battery Electrolyte to Form a Robust Anode–Electrolyte Nanointerface. *Nano Letters* **2021**, *21*, 8220-8228.

11. Nguyen, D.-T.; Eng, A. Y. S.; Ng, M.-F.; Kumar, V.; Sofer, Z.; Handoko, A. D.; Subramanian, G. S., et al., A High-Performance Magnesium Triflate-Based Electrolyte for Rechargeable Magnesium Batteries. *Cell Reports Physical Science* **2020**, *1*, 100265.

12. Wang, J.; Zhao, W.; Dou, H.; Wan, B.; Zhang, Y.; Li, W.; Zhao, X., et al., Electrostatic Shielding Guides Lateral Deposition for Stable Interphase toward Reversible Magnesium Metal Anodes. *ACS Applied Materials & Interfaces* **2020**, *12*, 19601-19606.

13. Wan, B.; Dou, H.; Zhao, X.; Wang, J.; Zhao, W.; Guo, M.; Zhang, Y., et al., Three-Dimensional Magnesiophilic Scaffolds for Reduced Passivation toward High-Rate Mg Metal Anodes in a Noncorrosive Electrolyte. *ACS Applied Materials & Interfaces* **2020**, *12*, 28298-28305.

14. Keyzer, E. N.; Lee, J.; Liu, Z.; Bond, A. D.; Wright, D. S.; Grey, C. P., A General Synthetic Methodology to Access Magnesium Aluminate Electrolyte Systems for Mg Batteries. *Journal of Materials Chemistry A* **2019**, *7*, 2677-2685.

15. Du, A.; Zhang, H.; Zhang, Z.; Zhao, J.; Cui, Z.; Zhao, Y.; Dong, S., et al., A Crosslinked Polytetrahydrofuran-Borate-Based Polymer Electrolyte Enabling Wide-Working-Temperature-Range Rechargeable Magnesium Batteries. *Advanced Materials* **2019**, *31*, 1805930.

16. Dou, H.; Zhao, W.; Zhao, X.; Wang, X.; Yang, X., Micro-Selection and Macro-Orientation Strategy Enables High-Areal-Capacity Magnesium Metal Anode. *ACS Energy Letters* **2024**, *9*, 800-809.

17. Zhao, Q.; Stalin, S.; Archer, L. A., Stabilizing Metal Battery Anodes through the Design of Solid Electrolyte Interphases. *Joule* **2021**, *5*, 1119-1142.

18. Luo, J.; He, S.; Liu, T. L., Tertiary Mg/$MgCl_2$/$AlCl_3$ Inorganic Mg^{2+} Electrolytes with Unprecedented Electrochemical Performance for Reversible Mg Deposition. *ACS Energy Letters* **2017**, *2*, 1197-1202.

19. Liu, T.; Shao, Y.; Li, G.; Gu, M.; Hu, J.; Xu, S.; Nie, Z., et al., A Facile Approach Using Mgcl2 to Formulate High Performance Mg^{2+} Electrolytes for Rechargeable Mg Batteries. *Journal of Materials Chemistry A* **2014**, *2*, 3430-3438.

20. He, Y.; Li, Q.; Yang, L.; Yang, C.; Xu, D., Electrochemical-Conditioning-Free and Water-Resistant Hybrid $AlCl_3$/$MgCl_2$/$Mg(TFSI)_2$ Electrolytes for Rechargeable Magnesium Batteries. *Angewandte Chemie International Edition* **2019**, *58*, 7615-7619.

21. Bhaghavathi Parambath, V.; Zhao-Karger, Z.; Diemant, T.; Jäckle, M.; Li, Z.; Scherer, T.; Gross, A., et al., Investigation on the Formation of Mg Metal Anode/Electrolyte Interfaces in Mg/S Batteries with Electrolyte Additives. *Journal of Materials Chemistry A* **2020**, *8*, 22998-23010.

22. Jeon, A.-R.; Jeon, S.; Lim, G.; Jang, J.; No, W. J.; Oh, S. H.; Hong, J., et al., Reversible Magnesium Metal Cycling in Additive-Free Simple Salt Electrolytes Enabled by Spontaneous Chemical Activation. *ACS Nano* **2023**, *17*, 8980-8991.

23. Dou, H.; Zhao, X.; Zhang, Y.; Zhao, W.; Yan, Y.; Ma, Z.-F.; Wang, X., et al., Revisiting the Degradation of Solid/Electrolyte Interfaces of Magnesium Metal Anodes: Decisive Role of Interfacial Composition. *Nano Energy* **2021**, *86*, 106087.

24. Chinnadurai, D.; Lieu, W. Y.; Kumar, S.; Yang, G.; Li, Y.; Seh, Z. W., A Passivation-Free Solid Electrolyte Interface Regulated by Magnesium Bromide Additive for Highly Reversible Magnesium Batteries. *Nano Letters* **2023**, *23*, 1564-1572.

25. Li, X.; Liu, Q.; Wang, X.; Liu, J.; Cheng, M.; Hu, J.; Wei, T., et al., A Facile in Situ Mg Surface Chemistry Strategy for Conditioning-Free $Mg[AlCl_4]_2$ Electrolytes. *Electrochimica Acta* **2022**, *414*, 140213.
26. Saha, P.; Datta, M. K.; Velikokhatnyi, O. I.; Manivannan, A.; Alman, D.; Kumta, P. N., Rechargeable Magnesium Battery: Current Status and Key Challenges for the Future. *Progress in Materials Science* **2014**, *66*, 1-86.
27. Lu, Z.; Schechter, A.; Moshkovich, M.; Aurbach, D., On the Electrochemical Behavior of Magnesium Electrodes in Polar Aprotic Electrolyte Solutions. *Journal of Electroanalytical Chemistry* **1999**, *466*, 203-217.
28. Aurbach, D.; Weissman, I.; Gofer, Y.; Levi, E., Nonaqueous Magnesium Electrochemistry and Its Application in Secondary Batteries. *The Chemical Record* **2003**, *3*, 61-73.
29. Yang, G.; Li, Y.; Zhang, C.; Wang, J.; Bai, Y.; Lim, C. Y. J.; Ng, M.-F., et al., In Situ Formed Magnesiophilic Sites Guiding Uniform Deposition for Stable Magnesium Metal Anodes. *Nano Letters* **2022**, *22*, 9138-9146.
30. Li, Y.; Yang, G.; Zhang, C.; Lieu, W. Y.; Lim, C. Y. J.; Sun, S.; Wang, J., et al., Grain-Boundary-Rich Triphasic Artificial Hybrid Interphase toward Practical Magnesium Metal Anodes. *Advanced Functional Materials* **2023**, *33*, 2210639.
31. Yang, G.; Li, Y.; Wang, J.; Lum, Y.; Lim, C. Y. J.; Ng, M.-F.; Zhang, C., et al., Realizing Horizontal Magnesium Platelet Deposition and Suppressed Surface Passivation for High-Performance Magnesium Metal Batteries. *Energy & Environmental Science* **2024**, *17*, 1141-1152.
32. Ouyang, K.; Ma, D.; Zhao, N.; Wang, Y.; Yang, M.; Mi, H.; Sun, L., et al., A New Insight into Ultrastable Zn Metal Batteries Enabled by in Situ Built Multifunctional Metallic Interphase. *Advanced Functional Materials* **2022**, *32*, 2109749.
33. Guo, F.; Wu, C.; Chen, S.; Ai, X.; Zhong, F.; Yang, H.; Qian, J., Flaky and Dense Lithium Deposition Enabled by a Nanoporous Copper Surface Layer on Lithium Metal Anode. *ACS Materials Letters* **2020**, *2*, 358-366.
34. Chinnadurai, D.; Li, Y.; Zhang, C.; Yang, G.; Lieu, W. Y.; Kumar, S.; Xing, Z., et al., Chloride-Free Electrolyte Based on Tetrabutylammonium Triflate Additive for Extended Anodic Stability in Magnesium Batteries. *Nano Letters* **2023**, *23*, 11233-11242.
35. Merrill, L. C.; Schaefer, J. L., Electrochemical Properties and Speciation in $Mg(HMDS)_2$-Based Electrolytes for Magnesium Batteries as a Function of Ethereal Solvent Type and Temperature. *Langmuir* **2017**, *33*, 9426-9433.

36. Kim, S. S.; See, K. A., Activating Magnesium Electrolytes through Chemical Generation of Free Chloride and Removal of Trace Water. *ACS Applied Materials & Interfaces* **2021**, *13*, 671-680.

37. Chen, C.; Chen, J.; Tan, S.; Huang, X.; Du, Y.; Shang, B.; Qu, B., et al., Regulating Solvation Sheath by Introducing Multifunctional Fluoride Boronic Esters for Highly Efficient Magnesium Stripping/Plating. *Energy Storage Materials* **2023**, *59*, 102792.

38. Wang, C.; Huang, H.; Wu, X.; Yousaf, M.; Yan, M.; Jiang, Y., Interfacial Reconstruction toward Reversible Mg Anode in Conventional Electrolytes. *ACS Applied Materials & Interfaces* **2023**, *15*, 51126-51134.

39. Chen, S.; Chen, Q.; Ma, J.; Wang, J.; Hui, K. S.; Zhang, J., Interface Coordination Stabilizing Reversible Redox of Zinc for High-Performance Zinc-Iodine Batteries. *Small* **2022**, *18*, 2200168.

40. Wen, T.; Qu, B.; Tan, S.; Huang, G.; Song, J.; Wang, Z.; Wang, J., et al., Rational Design of Artificial Interphase Buffer Layer with 3d Porous Channel for Uniform Deposition in Magnesium Metal Anodes. *Energy Storage Materials* **2023**, *55*, 816-825.

41. Martin, W.; Tian, Y.; Xiao, J., Understanding Diffusion and Electrochemical Reduction of Li^+ Ions in Liquid Lithium Metal Batteries. *Journal of The Electrochemical Society* **2021**, *168*, 060513.

42. Du, Y.; Chen, Y.; Tan, S.; Chen, J.; Huang, X.; Cui, L.; Long, J., et al., Strong Solvent Coordination Effect Inducing Gradient Solid-Electrolyte-Interphase Formation for Highly Efficient Mg Plating/Stripping. *Energy Storage Materials* **2023**, *62*, 102939.

43. Xiao, J.; Zhang, X.; Fan, H.; Lin, Q.; Pan, L.; Liu, H.; Su, Y., et al., Cosolvent-Assisted Formation of Charged Ion-Solvent Clusters and Solid Electrolyte Interphase for High-Performance Magnesium Metal Batteries. *Advanced Energy Materials* **2022**, *12*, 2202602.

44. Wang, Y.; Sun, Y.; Zhang, D.; Pan, M.; Chen, Y.; Chen, S.; Zhang, S., et al., A Hauser-Base Modulated Boron-Based Electrolyte Empowering Superior Interfacial Chemistry in Rechargeable Magnesium Batteries. *Energy Storage Materials* **2024**, *65*, 103152.

45. Zhang, D.; Duan, S.; Liu, X.; Yang, Y.; Zhang, Y.; Ren, W.; Zhang, S., et al., Deeping Insight of Mg $(CF_3SO_3)_2$ and Comprehensive Modified Electrolyte with Ionic Liquid Enabling High-Performance Magnesium Batteries. *Nano Energy* **2023**, *109*, 108257.

46. Long, J.; An, Y.; Yang, Z.; Zhang, G.; Zhang, J.; Tan, S.; An, Q., Efficient Boron-Based Electrolytes Constructed by Anionic and Interfacial Co-Regulation for Rechargeable Magnesium Batteries. *Chemical Engineering Journal* **2023**, *461*, 141901.

47. Zhang, D.; Wang, Y.; Yang, Y.; Zhang, Y.; Zhao, Y.; Pan, M.; Sun, Y., et al., Constructing Efficient Mg $(CF_3SO_3)_2$ Electrolyte Via Tailoring Solvation and Interface Chemistry for High-Performance Rechargeable Magnesium Batteries. *Advanced Energy Materials* **2023**, *13*, 2301795.

48. Sun, Y.; Wang, Y.; Jiang, L.; Dong, D.; Wang, W.; Fan, J.; Lu, Y.-C., Non-Nucleophilic Electrolyte with Non-Fluorinated Hybrid Solvents for Long-Life Magnesium Metal Batteries. *Energy & Environmental Science* **2023**, *16*, 265-274.

49. Ge, X.; Song, F.; Du, A.; Sun, G.; Zhang, S.; Zhao, J.; Zhang, Q., et al., Stable Anion-Rectifying Poly (Alkoxide Magnesium) Electrolytes for Reversible Magnesium Metal Batteries. *ACS Energy Letters* **2023**, *8*, 3685-3692.

50. Xiao, J.; Zhang, X.; Fan, H.; Zhao, Y.; Su, Y.; Liu, H.; Li, X., et al., Stable Solid Electrolyte Interphase in Situ Formed on Magnesium-Metal Anode by Using a Perfluorinated Alkoxide-Based All-Magnesium Salt Electrolyte. *Advanced Materials* **2022**, *34*, 2203783.

51. Wang, J.; Yang, J.; Xiao, Q.; Zhang, J.; Li, T.; Jia, L.; Wang, Z., et al., In Situ Self-Assembly of Ordered Organic/Inorganic Dual-Layered Interphase for Achieving Long-Life Dendrite-Free Li Metal Anodes in Lifsi-Based Electrolyte. *Advanced Functional Materials* **2021**, *31*, 2007434.

52. Wang, X.; Li, Y.; Meng, Y. S., Cryogenic Electron Microscopy for Characterizing and Diagnosing Batteries. *Joule* **2018**, *2*, 2225-2234.

53. Zhang, Z.; Cui, Y.; Vila, R.; Li, Y.; Zhang, W.; Zhou, W.; Chiu, W., et al., Cryogenic Electron Microscopy for Energy Materials. *Accounts of Chemical Research* **2021**, *54*, 3505-3517.

54. Bai, X.; Huang, Q.; Wang, L.; Yang, R.; Su, Z.; Jiang, T., Cryo−Electron Microscopy, Powerful Assistant for Advancing Battery. *Journal of Alloys and Compounds* **2024**, *1004*, 175913.

55. Li, C.; Guha, R. D.; Shyamsunder, A.; Persson, K. A.; Nazar, L. F., A Weakly Ion Pairing Electrolyte Designed for High Voltage Magnesium Batteries. *Energy & Environmental Science* **2024**, *17*, 190-201.

56. Spotte-Smith, E. W. C.; Blau, S. M.; Barter, D.; Leon, N. J.; Hahn, N. T.; Redkar, N. S.; Zavadil, K. R., et al., Chemical Reaction Networks Explain Gas Evolution Mechanisms in Mg-Ion Batteries. *Journal of the American Chemical Society* **2023**, *145*, 12181-12192.

57. Du, A.; Zhang, Z.; Qu, H.; Cui, Z.; Qiao, L.; Wang, L.; Chai, J., et al., An Efficient Organic Magnesium Borate-Based Electrolyte with Non-Nucleophilic Characteristics for Magnesium–Sulfur Battery. *Energy & Environmental Science* **2017**, *10*, 2616-2625.

58. Li, R.; Zhang, R.; Liu, Q.; An, J.; Song, Y.; Deng, B.; Ma, Y., et al., Bifunctional Non-Nucleophilic Electrolyte Enables Long-Life Magnesium Batteries Via Elimination of Passive Film on Mg Anode. *Chemical Engineering Journal* **2023**, *462*, 141998.

59. Shterenberg, I.; Salama, M.; Yoo, H. D.; Gofer, Y.; Park, J.-B.; Sun, Y.-K.; Aurbach, D., Evaluation of $(CF_3SO_2)_2N^-$ (TFSI) Based Electrolyte Solutions for Mg Batteries. *Journal of The Electrochemical Society* **2015**, *162*, A7118.

60. Li, Y.; Cheng, M.; Liu, Q.; Wang, R.; Ma, W.; Li, X.; Hu, J., et al., Toward High-Performance Mg/S Batteries with M4-Assisted $Mg(AlCl_4)_2$/PYR_{14}TFSI/DME Electrolyte and MoS_2@ CMK/S Cathode. *Small* **2024**, *20*, 2307396.

61. Fan, H.; Zheng, Z.; Zhao, L.; Li, W.; Wang, J.; Dai, M.; Zhao, Y., et al., Extending Cycle Life of Mg/S Battery by Activation of Mg Anode/Electrolyte Interface through an Licl-Assisted $MgCl_2$ Solubilization Mechanism. *Advanced Functional Materials* **2020**, *30*, 1909370.

62. Xu, Y.; Li, W.; Zhou, G.; Pan, Z.; Zhang, Y., A Non-Nucleophilic Mono-Mg^{2+} Electrolyte for Rechargeable Mg/S Battery. *Energy Storage Materials* **2018**, *14*, 253-257.

63. Merrill, L. C.; Schaefer, J. L., The Influence of Interfacial Chemistry on Magnesium Electrodeposition in Non-Nucleophilic Electrolytes Using Sulfone-Ether Mixtures. *Frontiers in Chemistry* **2019**, *7*, 194.

64. Bhardwaj, R. K.; Bhattacharyya, A. J., Efficient Magnesium Plating and Stripping in DOL/DME-$Mg(HMDS)_2$-Based Electrolytes and Application in Mg/S Batteries. *ACS applied energy materials* **2021**, *4*, 14121-14128.

65. Horia, R.; Nguyen, D. T.; Eng, A. Y. S.; Seh, Z. W., Comparative Study of Conventional Electrolytes for Rechargeable Magnesium Batteries. *Batteries & Supercaps* **2022**, *5*, e202200011.

66. Xie, M.-L.; Wang, J.; Hu, C.-J.; Zheng, L.; Kong, H.-B.; Shen, Y.-B.; Chen, H.-W., et al., An Additive Incorporated Non-Nucleophilic Electrolyte for Stable Magnesium Ion Batteries. *Journal of Electrochemistry* **2022**, *28*, 1.

67. Cui, Z.; Chen, P.; Liu, Y.; Zhang, L.; Nie, J.; Shang, B.; Chen, C., et al., Efficient and Stable Magnesium Plating/Stripping in High-Capacity Novel Mg//$Ni_{0.6}Co_{0.4}Se_2$ Batteries Enabled by Interfacial Chemistry Modulation. *ACS Sustainable Chemistry & Engineering* **2024**, *12*, 3886-3898.

68. Xiao, J.; Zhang, X.; Fan, H.; Lin, Q.; Ng, Z. S.; Chen, W.; Zhang, Y., Releasing Free Anions by High Donor Number Cosolvent in Noncorrosive Electrolytes of Commercially Available Magnesium Salts. *ACS Applied Materials & Interfaces* **2024**, *16*, 17673-17682.

69. Yang, L.; Yang, C.; Chen, Y.; Pu, Z.; Zhang, Z.; Jie, Y.; Zheng, X., et al., Hybrid $MgCl_2/AlCl_3/Mg(TFSI)_2$ Electrolytes in Dme Enabling High-Rate Rechargeable Mg Batteries. *ACS Applied Materials & Interfaces* **2021**, *13*, 30712-30721.
70. Xu, Y.; Zhou, G.; Zhao, S.; Li, W.; Shi, F.; Li, J.; Feng, J., et al., Improving a Mg/S Battery with Ycl3 Additive and Magnesium Polysulfide. *Advanced Science* **2019**, *6*, 1800981.
71. Huang, X.; Wen, J.; Lei, J.; Huang, G.; Pan, F.; Li, L., Facile and Economic Synthesis of Robust Non-Nucleophilic Electrolyte for High-Performance Rechargeable Magnesium Batteries. *ACS Applied Materials & Interfaces* **2022**, *14*, 8906-8915.
72. Zhang, J.; Guan, X.; Lv, R.; Wang, D.; Liu, P.; Luo, J., Rechargeable Mg Metal Batteries Enabled by a Protection Layer Formed in Vivo. *Energy Storage Materials* **2020**, *26*, 408-413.
73. Long, J.; Tan, S.; Wang, J.; Xiong, F.; Cui, L.; An, Q.; Mai, L., Revealing the Interfacial Chemistry of Fluoride Alkyl Magnesium Salts in Magnesium Metal Batteries. *Angewandte Chemie* **2023**, *135*, e202301934.
74. Eaves-Rathert, J.; Moyer, K.; Zohair, M.; Pint, C. L., Kinetic-Versus Diffusion-Driven Three-Dimensional Growth in Magnesium Metal Battery Anodes. *Joule* **2020**, *4*, 1324-1336.
75. Adams, B. D.; Zheng, J.; Ren, X.; Xu, W.; Zhang, J.-G., Accurate Determination of Coulombic Efficiency for Lithium Metal Anodes and Lithium Metal Batteries. *Advanced Energy Materials* **2018**, *8*, 1702097.

Table of contents

Traditional $Mg(HMDS)_2$ electrolytes tend to heavily passivate the magnesium anode surface, hindering reversible Mg deposition. The incorporation of an OctylBr additive modifies the electrolyte, resulting in reversible Mg deposition. The additive promotes a planar morphology and facilitates the in-situ formation of a bromine-rich interface, enabling the electrolyte to undergo seamless cycling at high areal capacities with minimal overpotentials.